Monte Carlo dosimetry of a realistic multicellular model of follicular lymphoma in a context of radioimmunotherapy

Julien Bordes, Sébastien Incerti, Erick Mora-ramirez, Jonathan Tranel, Cédric Rossi, Christine Bezombes, Julie Bordenave, Manuel Bardiès, Richard Brown, Marie-claude Bordage

Monte Carlo dosimetry of a realistic multicellular model of follicular lymphoma in a context of radioimmunotherapy

Julien Bordes[a,b]*, Sébastien Incerti[c,d], Erick Mora-Ramirez[a,b,e], Jonathan Tranel[a,b], Cédric Rossi[a,b,f], Christine Bezombes[a,b], Julie Bordenave [a,b], Manuel Bardiès[a,b], Richard Brown[g], Marie-Claude Bordage[a,b]

[a] *CRCT, UMR 1037 INSERM, Université Paul Sabatier F-31037 Toulouse, France*

[b] *UMR 1037, CRCT, Université Toulouse III-Paul Sabatier, F-31037, France*

[c] *Université de Bordeaux, CENBG, UMR 5797, F-33170 Gradignan, France*

[d] *CNRS, IN2P3, CENBG, UMR 5797, F-33170 Gradignan, France*

[e] *Universidad de Costa Rica, Escuela de Física, CICANUM, San José, Costa Rica*

[f] *CHU Dijon, Hématologie Clinique, Hôpital François Mitterand, 21000 Dijon, France*

[g] *Institute of Nuclear Medicine, University College London, UK*

* *Corresponding author at:*

Centre de Recherches en Cancérologie de Toulouse

INSERM UMR 1037 / Université Toulouse III Paul Sabatier

2 avenue Hubert Curien CS 53717

31037 TOULOUSE CEDEX 1 FRANCE

E-mail addresses:

julien.j.bordes@gmail.com

incerti@cenbg.in2p3.fr

erick.mora@ucr.ac.cr

j.tranel@hotmail.fr

cedric.rossi@chu-dijon.fr

christine.bezombes@inserm.fr

julie.bordenave@inserm.fr

manuel.bardies@inserm.fr

richard.brown@ucl.ac.uk

marie-claude.bordage@inserm.fr

Keywords:

Small-scale dosimetry, realistic biological data, rituximab, Auger electrons, β^- particles.

Abstract:

Purpose. Tumors geometry and radiopharmaceutical biodistribution impact the energy deposition in targeted radionuclide therapy. However, small-scale dosimetry studies generally consider an artificial environment where the tumors are spherical and the radionuclides are homogeneously biodistributed. To bring realism, we developed a dosimetric methodology based on a three-dimensional *in vitro* model of follicular lymphoma incubated with rituximab, an anti-CD20 monoclonal antibody used in the treatment of non-Hodgkin lymphomas, which might be combined with a radionuclide. The effects of the realistic geometry and biodistribution on the absorbed dose were highlighted by comparison with literature data. Additionally, to illustrate the possibilities of this methodology, the effect of different radionuclides on the absorbed dose distribution delivered to the *in vitro* tumor were compared.

Methods. The starting point was a model named Multicellular Aggregates of Lymphoma Cells (MALC). Three MALCs of different dimensions and their rituximab biodistribution were considered. Geometry, antibody location and concentration were extracted from selective plane illumination microscopy. Assuming antibody radiolabeling with Auger electron (^{125}I and ^{111}In) and β^- particle emitters (^{177}Lu, ^{131}I and ^{90}Y), we simulated energy deposition in MALCs using two Monte Carlo codes: Geant4-DNA with “CPA100” physics models for Auger electrons emitters and Geant4 with “Livermore” physics models for β^- particles emitters.

Results. MALCs had ellipsoid-like shapes with major radii, r, of ~ 0.25, ~ 0.5 and ~ 1.3 mm. Rituximab was concentrated in the periphery of the MALCs. The absorbed doses delivered by ^{177}Lu, ^{131}I and ^{90}Y in MALCs were compared with literature data for spheres with two types of homogeneous biodistributions (on the surface or throughout the volume). Compared to the MALCs, the mean absorbed doses delivered in spheres with surface biodistributions were between 18% and 38% lower, while with volume biodistribution they were between 15% and 29% higher. Regarding the radionuclides comparison, the relationship between MALC dimensions, rituximab biodistribution and energy released per decay impacted the absorbed doses. Despite releasing less energy, ^{125}I delivered a greater absorbed dose per decay than ^{111}In in the r ~ 0.25 mm MALC ($6.78 \cdot 10^{-2}$ *vs.* $6.26 \cdot 10^{-2}$ µGy · Bq^{-1} · s^{-1}). Similarly, the absorbed doses per decay in the r ~ 0.5 mm MALC for ^{177}Lu ($2.41 \cdot 10^{-2}$ µGy · Bq^{-1} · s^{-1}) and ^{131}I ($2.46 \cdot 10^{-2}$ µGy · Bq^{-1} · s^{-1}) are higher than for ^{90}Y ($1.98 \cdot 10^{-2}$ µGy · Bq^{-1} · s^{-1}). Furthermore, radionuclides releasing more energy per decay delivered absorbed dose more uniformly thorough the MALCs. Finally, when considering the radiopharmaceutical effective half-life, due to the biological half-life of rituximab being best matched by the physical half-life of ^{131}I and ^{177}Lu compared to ^{90}Y, the first two radionuclides delivered higher absorbed dose.

Conclusion. In the MALCs considered, β^- emitters delivered higher and more uniform absorbed dose than Auger electron emitters. When considering radiopharmaceutical half-lives, ^{131}I and ^{177}Lu delivered absorbed doses higher than ^{90}Y. In view of real irradiation of MALCs, such a work may be useful to select suited radionuclides and to help explain the biological effects.

1 Introduction

In targeted radionuclide therapy (TRT), a tumor-seeking agent is combined with an emitter of short-range radiation, such as Auger electrons (typically inferior to 1 μm in water), α particles (inferior to 100 μm) and β^- particles (in the order of millimeters). The objective of this combination is to deliver in patients a lethal absorbed dose to tumor cells while minimizing the exposure of healthy tissues. Thus, the development and the evaluation of TRT requires small-scale dosimetry studies[1,2]. However, previous studies have been generally based on simplifying assumptions (*e.g.* [3–8]) owing to the lack of data at the submillimeter scale regarding the tumor geometry and the radionuclide biodistribution.

Firstly, tumors were generally supposed spherical, or, alternatively, ellipsoidal. Absorbed dose in spheres was found to be higher than in the ellipsoids of the same volume[9], emphasizing the influence of the geometry. Secondly, small-scale dosimetry calculations have regularly assumed a homogeneous radionuclide biodistribution, either at the surface or within the volume of the tumor. In practice, the targeting of a tumor is not homogeneous, partly due to the heterogeneous distribution of the receptors (*i.e.* the antigens). Thus, mathematical models of heterogeneous radionuclide biodistributions within the tumors have been studied[10–13]. As could be expected, these models led to absorbed doses significantly less uniform within the tumor compared to homogeneous biodistributions. Therefore, given the impact of both tumor geometry and radionuclide biodistribution, there are clear calls for the development of small-scale dosimetry based on realistic biological data.

In the context of radioimmunotherapy (RIT), a single *in vitro* cultured carcinoma cell was considered in order to reproduce the effect of its realistic geometry and monoclonal antibody biodistribution on the dosimetry[14]. These biological data were extracted from microscope images. Assuming antibody radiolabeling with iodine-125, the energy deposition in the cell was calculated with Monte Carlo simulations. However, the relevance of this work was limited since tumors targeted in RIT such as non-Hodgkin lymphoma (NHL) grow as multicellular three-dimensional structures. Thus, a single cell dosimetric model neglects the absorbed dose delivered by the radiopharmaceutical bound to other cells of the tumor (crossfire effect). Furthermore, studies regarding unlabeled monoclonal antibody treatments highlighted that the biodistribution might be impacted by the tumor size and the extracellular matrix

(*i.e.* the assemblage of non-cellular molecules providing structural support for the surrounding cells), limiting the effectiveness of the treatment. Increasing tumor size is regarded as possibly reducing the monoclonal antibody concentration and decreasing survival of a mouse model[15] and patients[16]. Furthermore, the extracellular matrix might hamper the monoclonal antibody penetration[17]. To address these questions, a three-dimensional *in vitro* culture system of follicular lymphoma (a NHL subtype) expressing extracellular matrix was designed in a separate project at the Cancer Research Center of Toulouse[18–21]. The model was termed multicellular aggregate of lymphoma cells (MALC). The MALCs were incubated with rituximab. This chimeric monoclonal antibody targeting the membrane-associated CD20 antigen has been combined with radionuclides for RIT treatments (see clinical review of Read *et al.*[22]).

To improve the realism and the relevance of the single cell dosimetry, this paper presents a dosimetric model based on selective plane illumination microscopy (SPIM) images of three MALCs, of different size, treated by rituximab. Data were extracted to define the tumor geometry and the radiopharmaceutical biodistribution. Rituximab was virtually radiolabeled with two types of electron emitters. The Auger electron emitters iodine-125 (^{125}I) and indium-111 (^{111}In) were studied because they proved their efficiency in destroying lymphoma cells *in vitro* in RIT-related research[23,24]. β^- particle emitters lutetium-177 (^{177}Lu), iodine-131 (^{131}I) and yttrium-90 (^{90}Y) were also considered. For the RIT treatment of patients with relapsed / refractory NHL, ^{177}Lu-lilotomab satetraxetan is currently on trial[25], while both ^{131}I-tositumomab (Bexxar) and ^{90}Y-ibritumomab tiuxetan (Zevalin) have been used[26]. In RIT, the dosimetry is highly impacted by the radiopharmaceutical effective half-life, a parameter that would depend on the rituximab radiolabeling. We studied the energy deposition patterns in MALCs with Monte Carlo modeling of radiation transport. Additionally, the effective half-life was accounted for by using the simulated data and a simple pharmacokinetic model.

As a first step, the relevance of implementing realistic biological data was highlighted by comparing average absorbed doses to literature data. For the following step, to illustrate the possibilities offered by this new dosimetric model, we compared the radionuclides' absorbed fraction, average absorbed dose and absorbed dose volume distribution. As a last step, the influence of the radiopharmaceuticals half-life on the absorbed dose was studied.

2 Material and methods

2.1 Three-dimensional model of follicular lymphoma

The development of the MALCs as well as the microscopy acquisition were detailed in prior studies[18–21]. This section focuses on information relevant to the present work.

2.1.1 MALC growth and labeling

To compare the antibody biodistribution in different tumor volumes, the MALCs, created with follicular lymphoma cells expressing green fluorescent protein (GFP), were cultured during 2, 5 or 10 days (hereafter referred to as D2, D5 and D10). Then, they were treated by a saturating concentration of 10 µg/ml of CF555 labeled rituximab[27] for a duration of 24 h.

2.1.2 SPIM imaging

Fluorescence microscopy technologies, such as SPIM detect the light emitted by fluorescent markers[28]. SPIM was particularly adapted to this study since it allows the observation of whole organisms or three-dimensional multicellular models over a few millimeters while keeping a low phototoxicity[29,30]. 24 h after rituximab administration, z-stack of images were acquired. Each image corresponded to a slice of the MALC in the x-y plane. For example, Figure 1 displays a central slice of MALCs (a) D2, (b) D5 and (c) D10. Green signal corresponds to GFP 488 nm emission and reveals MALC geometry. The black hollow at the center of MALCs D5 and D10 are due to a lack of follicular lymphoma cells. Red signal from the 561 nm emission of CF555 represents the rituximab biodistribution. To optimize the contrast between follicular lymphoma cells and rituximab, the colors on the images differ from the real colors produced by the fluorescent markers. SPIM images were composed of voxels with (x, y and z) dimensions of $3.7 \cdot 3.7 \cdot 3.1$ µm^3 and were stored into TIFF files.

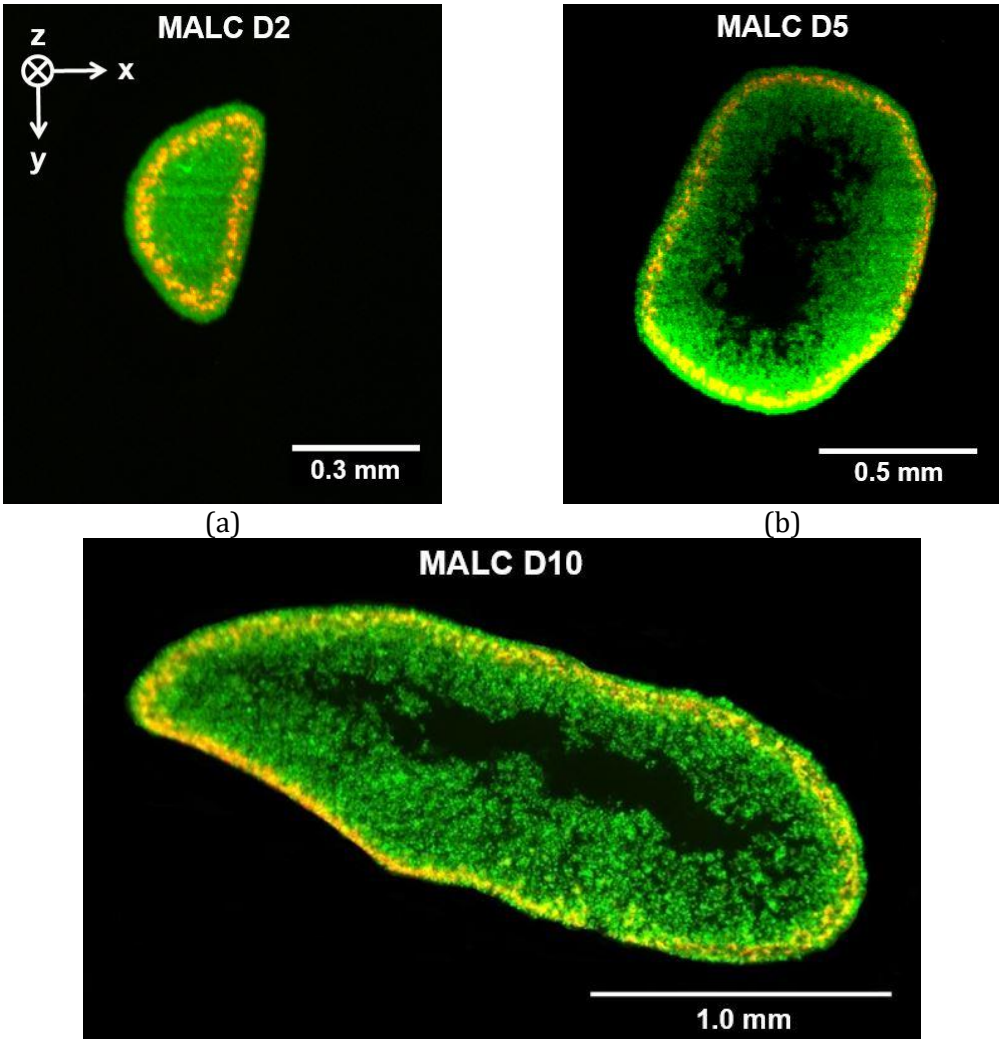

Figure 1. SPIM images of the central slices of the MALC: (a) D2, (b) D5 and (c) D10. Follicular lymphoma cell nuclei and rituximab appear in green and red, respectively.

2.2 Image processing

To extract the data required for the dosimetry of the MALCs, SPIM images were processed with Fiji[31] ("Fiji Is Just ImageJ", downloadable from fiji.sc). This program has specific features for the processing of microscope images of three-dimensional biological samples[32] and can read TIFF files. First, the stacks of images were transferred to Fiji for 3D reconstructions (*e.g.* MALC D5 in Figure 2). Then, two macros were developed and implemented in Fiji:

- The first one treated the green signal in order to extract the MALCs geometry. MALC voxels were separated from the background by applying an intensity threshold. A clear delineation of the MALCs boundary allowed a straightforward determination of the threshold value. Since the black hollow sections of the MALC D5 and D10 were in the center, they were considered as a part of the volume of interest (VOI). Finally, in view of the definition of the MALC geometry during Monte Carlo simulations,

the macro recorded different information into a ".dat" file; namely, the number of voxels, the voxel dimensions along the three axes, and each voxel coordinate (x, y, z).

- The second macro treated the red signal from the rituximab CF555 label. It removed the background noise, then recorded the voxel coordinates and intensity into a ".dat" file. During simulations, the source voxels were selected with a probability directly derived from their red signal intensity. It was supposed that the CF555 biodistribution would be identical to the radiopharmaceutical. This assumes that the CF555 labeling would neither detach from the antibody nor impact its biodistribution. To the best of our knowledge, no publication addresses these questions. This also assumes that the radiolabeling would not affect the rituximab biodistribution. This last point is supported by the requirement that, in nuclear medicine, the radiolabeling strategies preserve the biological properties of the proteins[33] such as rituximab.

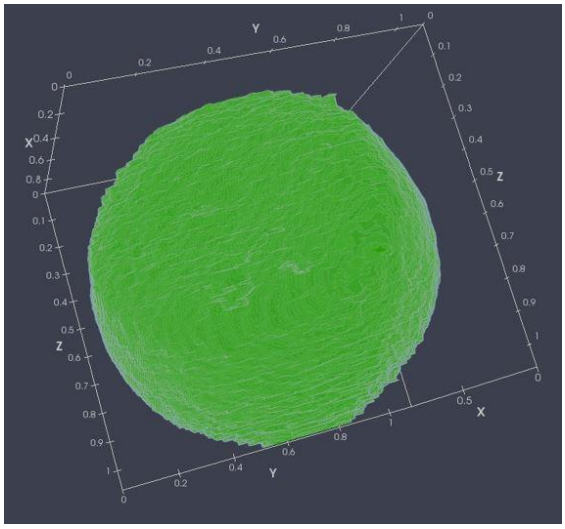

Figure 2. 3D reconstruction of MALC D5 from SPIM images. The axes are given in millimeters.

2.3 Voxel-based dosimetry

2.3.1 General settings

Energy depositions were calculated with the Geant4 Monte Carlo open-source platform[34–36] since it enables the implementation of voxelized geometries and its physics models are well adapted to energies encountered in TRT. Furthermore, Geant4, being a well-established object-oriented code base, has a high degree of reuse meaning that little code must be written for a new application. The Geant4

"microbeam" example served as a basis. It was developed at the Centre d'Études Nucléaires de Bordeaux-Gradignan (CENBG) to simulate the irradiation of individual cells with a microbeam of protons or α particles[37,38]. In order to suit this example for TRT, we added the possibility of simulating the irradiation of a VOI (in this work the MALC) by internalized radiopharmaceuticals. To reconstruct the MALCs, the class *G4PVParameterised* placed the SPIM images voxels ($3.7 \cdot 3.7 \cdot 3.1$ μm^3) according to their coordinates stored in the output file of the first macro (see 2.2). The MALCs were positioned into a sphere of liquid water. This enabled electron backscattering into the MALCs with the consequence of an additional energy deposition. The simulation of the irradiation of each MALC by each radionuclide considered 10^6 decays. The activity was assumed homogeneously biodistributed within a voxel source. Accordingly, the coordinates of a decay site inside such a voxel were sampled from a uniform distribution. The particles were then emitted isotropically. Depending on the type of electron emitter, energy depositions in the MALCs were simulated with different methods that will be presented in the following sections (2.3.2 and 2.3.3).

2.3.2 Auger electron emitters

^{125}I and ^{111}In mean emission spectra of monoenergetic electrons (Auger and internal conversion electrons, Figure 3) and photons (X-rays and γ-rays) were extracted from the publication of the American Association of Physicists in Medicine[39] (AAPM), as it is still a reference for Auger electron emitters (*e.g.* [14,40,41]). Table 1 shows important properties of the decay of ^{125}I and ^{111}In. Half-lives were extracted from the Medical Internal Radiation Dose (MIRD) book[42]. The mean penetration corresponds to the length of the vector connecting the electron emission and stopping points. Hence, this distance is lower than the path length because the latter considers the direction changes of the electrons. Although nuclear medicine dosimetric studies usually report the path length, in the present work the penetration was more relevant for analyzing the results.

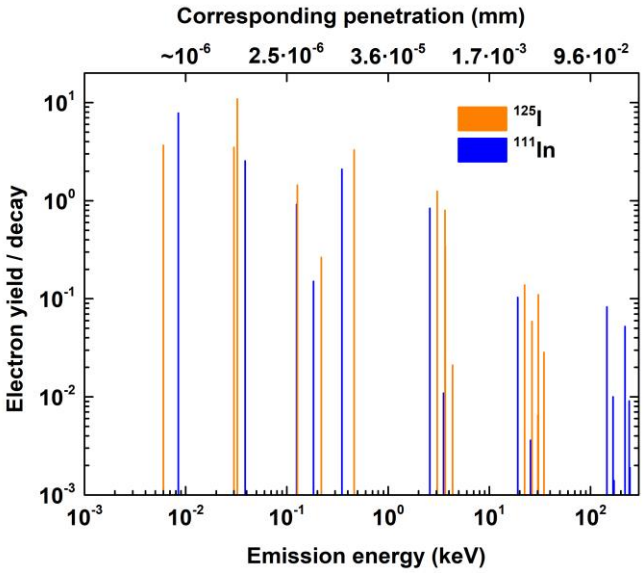

Figure 3. Mean electron emission spectra (Auger and internal conversion electrons) of ^{125}I and ^{111}In from the AAPM publication[39]. For each energy decade, the top x-axis provides the corresponding mean penetration according to Geant4-DNA.

Table 1. Some physical properties of the Auger electron emitters. Half-lives come from MIRD data[42], spectra data were extracted from the AAPM publication[39] and mean penetrations were determined with Geant4-DNA.

Auger electron emitter	**^{125}I**	**^{111}In**
Half-life (day)	59.4	2.8
Mean electron energy released (keV/decay)	19.5	34.7
Electron yield per decay	25.8	14.9
Electron mean energy $E_{e^-\,mean}$ (keV)	0.8	2.3
Penetration at $E_{e^-\,mean}$ (mm)	$2.5 \cdot 10^{-5}$	$1.4 \cdot 10^{-4}$
Maximum energy $E_{e^-\,max}$ (keV)	34.7	245.0
Penetration at $E_{e^-\,max}$ (mm)	$1.5 \cdot 10^{-2}$	$4.2 \cdot 10^{-1}$

Auger electrons induce energy deposition clusters localized at the nanometer scale[43]. Such phenomena can be studied with step-by-step Monte Carlo codes since they give the track structure of the particles down to the nanometer scale. Accordingly, ^{125}I and ^{111}In emissions were simulated with Geant4-DNA[44–47] (geant4-dna.org). "CPA100" physics models ("option 6")[48,49] were used. They describe ionization, electronic excitation and elastic scattering processes and are applicable from 256 keV down to 11 eV in liquid water.

For the simulations of photon interactions (Compton and Rayleigh scatterings as well as photo-electric absorption), Geant4-DNA does not provide any physics models to-date. Thus, Geant4 "Livermore" physics models for photons were selected[50,51]. During simulations, electrons and photons could produce vacancies in the atomic shells so atomic deexcitation emission was tracked (Auger electron emission, Auger cascade and fluorescence).

2.3.3 β^- particle emitters

AAPM's publication[39] only provides data for Auger electron emitters. Therefore, ^{177}Lu, ^{131}I and ^{90}Y mean emission spectra of β^- particles (Figure 4), monoenergetic electrons and photons were extracted from the MIRD book[42]. Table 2 presents the main properties of the decay of ^{177}Lu, ^{131}I and ^{90}Y.

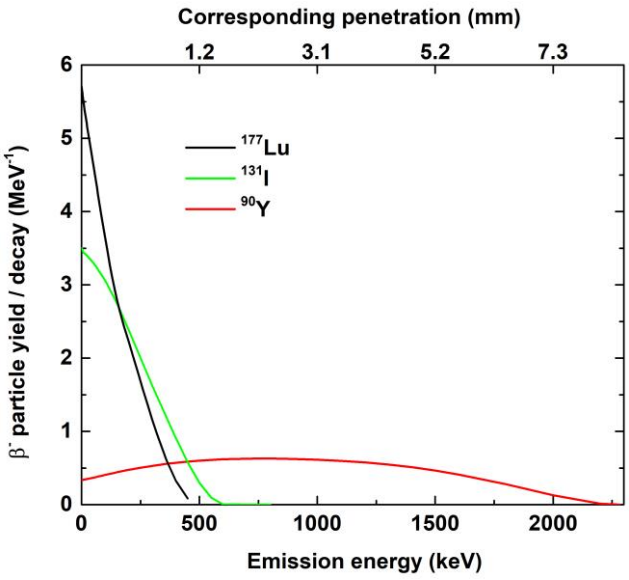

Figure 4. β^- particle emission spectra of ^{177}Lu, ^{131}I and ^{90}Y from MIRD book[42]. The top x-axis provides the corresponding Geant4 mean penetration every 500 keV.

Table 2. Some physical properties of the β- particle emitters. Half-lives and spectra data come from MIRD book[42] and mean penetrations were determined with Geant4.

β- particle emitter	**^{177}Lu**	**^{131}I**	**^{90}Y**
Half-life (day)	6.6	8.0	2.7
Mean electron energy (β- particles + monoenergetic electrons) released (keV/decay)	147.8	191.7	933.2
β- particle mean energy $E_{\beta^-_{mean}}$ (keV)	133.1	181.8	933.0
Penetration at $E_{\beta^-_{mean}}$ (mm)	$1.6 \cdot 10^{-1}$	$2.6 \cdot 10^{-1}$	2.9
β- particle maximum energy $E_{\beta^-_{max}}$ (keV)	497.8	806.9	2280.1
Penetration at $E_{\beta^-_{max}}$ (mm)	1.2	2.4	8.4

Part of the emission of ^{177}Lu, ^{131}I and ^{90}Y has an energy too high to be modeled with Geant4-DNA physics models. Thus, simulations of the irradiation with these emitters were accomplished with Geant4 in a condensed history mode, as this provides physics models applicable up to GeV energies. "Livermore"[52,53] physics models were used to describe particles interactions.

The ionization process was simulated along with bremsstrahlung. This latter slightly increased the stopping power of the electrons / β- particles at these energies, thus marginally reducing their penetration. "Livermore" electron models are defined down to about 10 eV. Nevertheless, in accordance with guidelines, the cut-off was set to 250 eV. Energy production cuts for secondary particles was also fixed at 250 eV. In order to limit the number of electrons crossing a voxel with no energy deposition, step size limit was arbitrary chosen to 0.6 µm, corresponding to less than 1/5 of the voxel dimensions.

2.4 Dosimetric quantities

2.4.1 Simulation results

Geant4 simulations generated output files containing the energy deposited in the MALCs voxels. Firstly, different dosimetric quantities were directly calculated from these data: the absorbed fraction and the absorbed dose.

241 - The absorbed fraction ϕ represents the fraction of energy released from the source region that
242 is deposited in the target region. Here, the MALCs represent both the source and the target regions. The
243 results focused on electron absorbed fractions ϕ_{e^-} (monoenergetic electrons and eventually β^- parti-
244 cles), because photon absorbed fractions are insignificant at this scale:

$$\phi_{e^-\,MALC} = \frac{E_{e^-}}{E_{e^-\,0}} \quad (1)$$

245 Where E_{e^-} is the deposited energy and $E_{e^-\,0}$ the electron-released energy. The absorbed fraction
246 is frequently reported in nuclear medicine dosimetry studies[54].

247 - The energy deposited E_i (in J) in a VOI i (either a whole MALC or a voxel) characterized by a
248 mass m_i (in kg) was converted to absorbed dose D_i (in Gy):

$$D_i = \frac{E_i}{m_i} \quad (2)$$

249 This quantity was then divided by 10^6 to obtain the mean absorbed dose per decay (or per unit
250 of time-integrated activity, in Bq · s, according to MIRD most recent terminology[55]). First, this quantity
251 was determined for the whole MALCs. However, the absorbed dose was not uniformly delivered within
252 the volume. In order to specify the volume fractions having received either low or high absorbed dose,
253 cumulative dose-volume histograms (cDVH) were plotted. They give the fraction of the volume (*i.e.* the
254 fraction of MALC voxels) in which an absorbed dose greater than or equal to a given value was delivered.
255 These graphs are routinely used in external radiotherapy, but also in some TRT studies[56,57].

256 **2.4.2 Considering radiopharmaceutical effective half-life**

257 Subsequently, in order to consider the effective half-life of the radiopharmaceutical X-rituximab
258 (X being one of the radionuclides), the MALCs and voxels absorbed doses per unit administered activity
259 (A_0 in Bq) were calculated. In nuclear medicine, this quantity allows the assessment of the absorbed
260 dose delivered to a VOI for a given administered activity. It was calculated as the product of the absorbed
261 doses per decay (see 2.4.1) and the time-integrated activity coefficient ã (also known as the residence
262 time and given in s). The value of ã represents the total number of decays occurring in a MALC per unit
263 administered activity[55]:

$$\tilde{a} = \frac{1}{A_0} \int_0^{\infty} A(X - \text{rituximab}, t) \cdot dt \quad (3)$$

Where $A(X - \text{rituximab}, t)$ is the time-dependent activity of the radiopharmaceutical in a MALC (in Bq). Assuming that this radiopharmaceutical has an instantaneous uptake in a MALC (*i.e.* instantaneously bound to the MALCs according to the biodistribution extracted from the images) and its elimination is monoexponential:

$$\tilde{a} = \frac{1}{A_0} \int_0^{\infty} A_0 \cdot e^{-(\ln(2)/T_{eff}(X-\text{rituximab}))\cdot t} \cdot dt \quad (4)$$

$$\tilde{a} = 1.443 \cdot T_{eff}(X - \text{rituximab}) \quad (5)$$

Where $T_{eff}(X - \text{rituximab})$, the effective half-life of the radiopharmaceutical (in s), depends on $T_{phys}(X)$ the physical half-life of the radionuclide X (in s) and on $T_{bio}(\text{rituximab})$ the biological half-life of rituximab (in s):

$$T_{eff}(X - \text{rituximab}) = \frac{T_{phys}(X) \cdot T_{bio}(\text{rituximab})}{T_{phys}(X) + T_{bio}(\text{rituximab})} \quad (6)$$

The physical half-lives are well documented (see Table 1 and Table 2), but, rituximab biological half-life in NHL is less-well established. In a clinical study, Scheidhauer *et al.* evaluated the effective half-life of the radiopharmaceutical ^{131}I-rituximab in NHL[58]. Biodistribution in 14 patients was determined by gamma camera imaging. Our work focused on the 3.4 days mean effective half-life determined by Scheidhauer *et al*. We emphasize, however, that its precision is limited. It is associated to a standard deviation of 1.1 day. Also, Scheidhauer *et al.* reported a high inter-patient variability, with effective half-lives ranging from 1.7 to 5.5 days. The gamma camera imaging introduces further uncertainties on the dosimetry[59-60]. According to equation (6), the 3.4 days effective half-life corresponds to a rituximab biological half-life of 5.8 days. Using this value and the equation (6), the effective half-lives of rituximab radiolabeled with ^{125}I, ^{111}In, ^{177}Lu or ^{90}Y were deducted.

3 Results

3.1 MALC and rituximab biodistribution characteristics

Table 3 presents the dimensions of the three MALCs along x-, y-, z- axes and their masses in Geant4 simulations which were used to determine the absorbed doses according to equation (2). The masses were evaluated by multiplying the number of voxels in a MALC by the mass of a voxel filled with liquid water (as simulations were performed in this material). Figure 1 shows that MALCs considered in this study have ellipsoid-like shape. For MALC D2, D5 and D10, major radii are ~0.25 mm, ~0.5 mm and ~1.3 mm, respectively. Rituximab is heterogeneously biodistributed inside a shell-like volume at the periphery of the MALCs (Figure 1). Generally, the shell-like volumes are characterized by a thickness and a distance to the surface of the MALCs both of the order of a few hundredths of a millimeter. It was previously demonstrated that the extracellular matrix limits the diffusion of therapeutic agents in tumors[17]. It was also shown that MALCs expressed extracellular matrix proteins[20]. Accordingly, in an ongoing MALC-based study, the possibility that the rituximab peripheral location is due to the extracellular matrix is being investigated.

Table 3. Sizes along x-, y- and z-axes of the MALCs D2, D5 and D10.

MALC	Dimensions x · y · z (mm^3)	Mass (mg)
D2	$0.34 \cdot 0.53 \cdot 0.50$	$4.6 \cdot 10^{-2}$
D5	$0.96 \cdot 1.09 \cdot 1.07$	$5.5 \cdot 10^{-1}$
D10	$2.54 \cdot 1.23 \cdot 2.26$	2.8

3.2 Dosimetric quantities per decay

3.2.1 Comparison with literature data obtained in a simplified model

Figure 5 displays the relative difference (%) of absorbed dose per decay between the reference data of Bardiès and Chatal[3] for spheres with either (a) a surface or (b) a volume biodistribution and MALCs calculations (relative difference = $100 \cdot (D_{sphere} - D_{MALC}) / D_{MALC}$). In this previous study, calculations were carried out by an analytical method based on scaled dose-point kernels in spheres with radius ranging from 0.01 to 22 mm. For a valid comparison, the results for a MALC were compared to the results of the sphere having the closest mass. Accordingly, absorbed doses for MALCs D2, D5 and D10

were compared to the values for spheres with radius, r, of 0.2 mm, 0.5 mm and 0.9 mm, respectively. Furthermore, only ^{177}Lu, ^{131}I and ^{90}Y were considered because Bardiès and Chatal focused their study on β^- particle emitters. The peripheral biodistribution of rituximab (discussed in section 3.1) can be seen as an intermediate between the surface and volume biodistributions assumed by Bardiès and Chatal. Hence, this is coherent that the absorbed doses per decay for MALCs lie between the values for these two theoretical situations. It is also noticeable that results with these two biodistributions own a similar degree of agreement with results for the MALCs. This indicates that for the purpose of absorbed dose calculations, in these particular cases, the surface and the volume biodistribution are both equally relevant. Furthermore, non-negligible discrepancies between the theoretical model and realistic data were observed. These results highlight the need to account of realistic biological data.

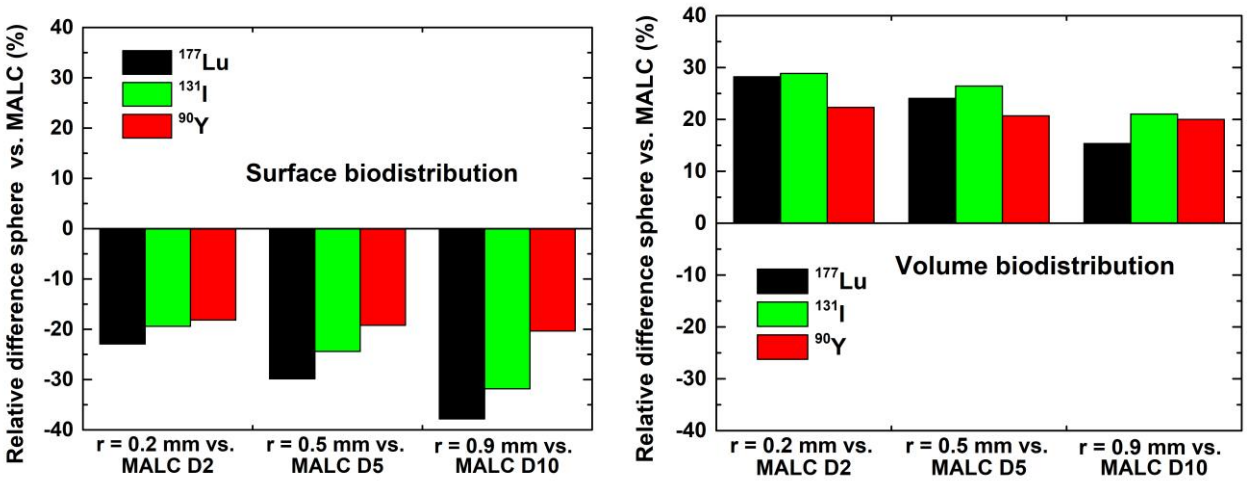

(a) (b)

Figure 5. Relative differences (%) between absorbed dose per decay calculated in spheres of various radii with either a (a) surface or (b) a volume biodistribution[3] and MALCs (taken as reference). Comparison spheres *vs.* MALCs are as follow: r = 0.2 mm *vs.* MALC D2 (left), r = 0.5 mm *vs.* MALC D5 (middle) and r = 0.9 mm *vs.* MALC D10 (right).

3.2.2 Comparison of the radionuclides

For clarity, the results for each radionuclide are reported by ascending order of energy released per decay, that is: ^{125}I, ^{111}In, ^{177}Lu, ^{131}I and ^{90}Y.

Figure 6 displays, for each radionuclide, the electron absorbed fraction in the MALCs and Table 4 shows the corresponding numerical values. As MALCs get bigger, the electrons / β^- particles deposit

more energy inside before exiting them, increasing the absorbed fractions. Assuming a homogeneous surface biodistribution of rituximab (which is at first sight the closer approximation of the real biodistribution as seen on Figure 1), for very large MALCs the absorbed fraction would tend toward 0.5 (semi-infinite medium condition). However, for MALC D5 and D10, the values become greater than 0.5 for all radionuclides but ^{90}Y (presumably, absorbed fraction of ^{90}Y would become greater than 0.5 in bigger MALCs). This can be explained by the rituximab penetration inside the MALCs, enabling the electrons / β^- particles to systematically deposit energy in the VOI, regardless their trajectories. This point is critical since it further demonstrates the importance of using realistic biological data.

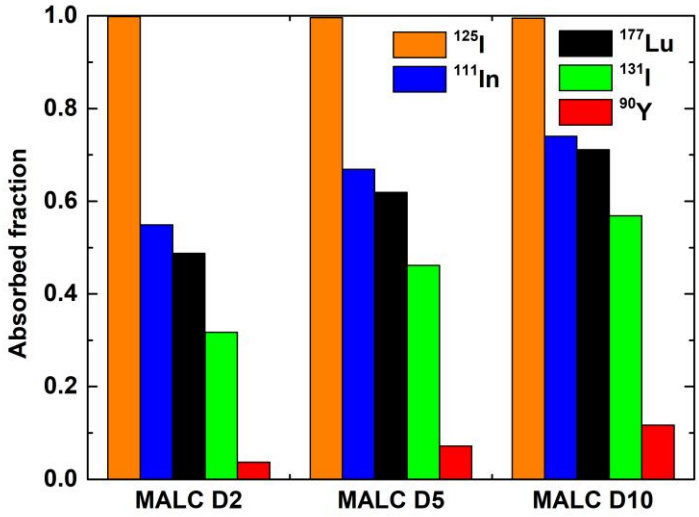

Figure 6. Absorbed fractions in MALCs D2, D5 and D10 for ^{125}I, ^{111}In, ^{177}Lu, ^{131}I and ^{90}Y.

Table 4. Absorbed fraction in the MALCs for the five radionuclides.

	Absorbed fraction		
Radionuclide	**MALC D2**	**MALC D5**	**MALC D10**
^{125}I	1.00	1.00	1.00
^{111}In	0.55	0.67	0.74
^{177}Lu	0.49	0.62	0.71
^{131}I	0.32	0.46	0.57
^{90}Y	0.04	0.07	0.12

As radionuclides release more energy per decay, the penetration of the electrons / β^- particles increase (see Table 1 and Table 2). Thus, more energy is deposited outside the MALCs, and in turn the

absorbed fractions decrease. ^{125}I deposits nearly its whole electron energy within the three MALCs. The electrons it emits are unlikely to deposit energy outside the MALCs since their penetrations are limited to $1.5 \cdot 10^{-2}$ mm while the rituximab is mostly located at more than $\sim 3 \cdot 10^{-2}$ mm from the edge. Note that the real values are inferior to 0.998 (rounded to 1.00 for consistency), due to scarce rituximab biodistribution closer to or at the surface. The absorbed fractions for ^{111}In, lying between 0.55 and 0.74, are notably lower than that of ^{125}I. The reason is that ~80% of the electron energy released per decay of ^{111}In is taken away by emissions of at least 145.0 keV, characterized by penetrations above $1.8 \cdot 10^{-1}$ mm (right-hand side of Figure 3). Due to this property, the absorbed fractions for ^{111}In are remarkably close to ^{177}Lu, as their emissions have similar penetrations. Furthermore, the absorbed fractions for ^{131}I are higher than for ^{177}Lu as its penetration are higher (by $1.0 \cdot 10^{-1}$ mm at $E_{\beta^- mean}$). Finally, the absorbed fractions for ^{90}Y, ranging between 0.04 and 0.12, are by far the lowest. Such low values are due to the penetrations of its emissions (up to 8.4 mm) being significantly superior to the size of the MALCs.

Figure 7 displays the mean absorbed dose per decay delivered to the MALCs by each radionuclide and Table 5 shows the corresponding numerical values. These results are impacted by the energy released by the radionuclides and the absorbed fractions.

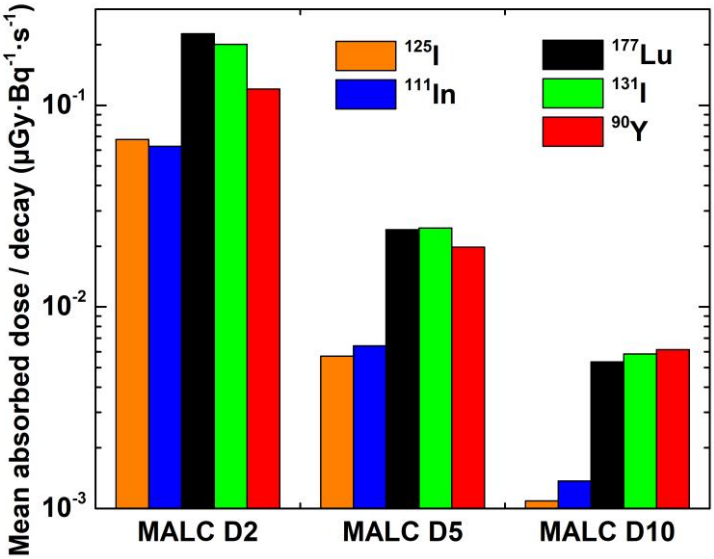

Figure 7. Mean absorbed dose per decay in MALC D2, D5 and D10 for ^{125}I, ^{111}In, ^{177}Lu, ^{131}I and ^{90}Y.

Table 5. Mean absorbed dose per decay in the MALCs for the five radionuclides.

	Mean absorbed dose per decay (μGy · Bq^{-1} · s^{-1})		
Radionuclide	**MALC D2**	**MALC D5**	**MALC D10**
^{125}I	$6.78 \cdot 10^{-2}$	$5.69 \cdot 10^{-3}$	$1.10 \cdot 10^{-3}$
^{111}In	$6.26 \cdot 10^{-2}$	$6.41 \cdot 10^{-3}$	$1.37 \cdot 10^{-3}$
^{177}Lu	$2.27 \cdot 10^{-1}$	$2.41 \cdot 10^{-2}$	$5.34 \cdot 10^{-3}$
^{131}I	$2.01 \cdot 10^{-1}$	$2.46 \cdot 10^{-2}$	$5.84 \cdot 10^{-3}$
^{90}Y	$1.21 \cdot 10^{-1}$	$1.98 \cdot 10^{-2}$	$6.15 \cdot 10^{-3}$

Despite ^{111}In (34.7 keV/decay) releasing more energy than ^{125}I (19.5 keV/decay), the former delivered a lower absorbed dose in MALC D2 due to its lower absorbed fraction. Nevertheless, for MALC D5 and D10, the absorbed fraction for ^{111}In increases, leading to greater absorbed doses than for ^{125}I.

In each MALC, absorbed doses for β^- particle emitters are greater than for Auger electron emitters, because they release considerably more energy. For example, absorbed doses for ^{177}Lu are greater than that of ^{111}In by a factor ~4. Both have similar absorbed fractions, but ^{177}Lu (147.8 keV/decay) releases ~4 times more energy. For β^- particle emitters, ^{177}Lu and ^{131}I (191.7 keV/decay) results are close. Lower energy released by ^{177}Lu, is compensated by its higher absorbed fractions. Among β^- particle emitters, ^{90}Y (933.2 keV/decay) emits by far the more energy, yet the absorbed doses delivered are lowest in MALCs D2 and D5 due to extremely low absorbed fractions. In MALC D10, however, it delivered the highest absorbed doses because, compared to MALC D2, absorbed fractions were increased by a factor 3.

Figure 8 illustrates, as an example the distributions of the absorbed dose per decay (in μGy·Bq^{-1}·s^{-1}) inside the voxels of the slice of MALC D5 shown in Figure 1 (b). Note that 0.01 μGy·Bq^{-1}·s^{-1} corresponds to a mean energy deposited per decay inside a voxel of $2.6 \cdot 10^{-3}$ eV·Bq^{-1}·s^{-1}. Figure 9 displays the cDVH (in μGy·Bq^{-1}·s^{-1}) of MALCs (a) D2, (b) D5 and (c) D10 for ^{125}I, ^{111}In, ^{177}Lu, ^{131}I and ^{90}Y. Globally, when radionuclides release more energy, the absorbed dose is delivered more uniformly within the MALCs because of the increasing penetration of the emission.

Figure 8 (b) highlights the peripheral irradiation of ^{125}I, with a pattern very similar to the rituximab biodistribution. However, this radionuclide delivered high absorbed dose as revealed by the less-steep gradient of its cDVH. These observations are consistent with ^{125}I emitting low energy electrons, which deposit most of the energy in a small distance from the decay site. The highly localized absorbed dose delivered by ^{125}I was further observed at the cellular level by Arnaud *et al.*[14]. Unlike this radionuclide, ^{111}In sparsely delivered absorbed dose in the central part of the MALCs (Figure 8 (c)) due to the higher penetrations of its emission. For both Auger electron emitters, the low absorbed dose delivered in the central part of the MALCs (or the lack thereof) is linked to the rituximab peripheral biodistribution. Nevertheless, the limited penetration of rituximab inside the MALCs can be counterbalanced by a radiolabeling with one of the β$^-$ particle emitters.

This benefit, illustrated by Figure 8 (d), (e) and (f), was brought by the higher penetration of their emission. It translates to higher cDVH values on the left-hand side (Figure 9). Among β$^-$ particle emitters, ^{90}Y energy deposition was the most uniform throughout the MALCs. In comparison, ^{177}Lu and ^{131}I deposited less energy in the central part but more in the periphery. The improved absorbed dose uniformity of ^{90}Y is further expressed by steeper gradients in its cDVH. It is linked to the variation of penetration and stopping power of β$^-$ particles with their energy. β$^-$ particles emitted by ^{90}Y having higher penetrations than for ^{177}Lu and ^{131}I, were more likely to reach the center of the MALCs. This difference is more pronounced as MALCs get bigger. Compared to ^{177}Lu and ^{131}I, emissions of ^{90}Y have lower stopping powers (according to NIST database[61], at $E_{\beta^-_{mean}}$: 0.34, 0.29 and 0.19 keV/µm, respectively), thus they deposited less energy close to the decay site.

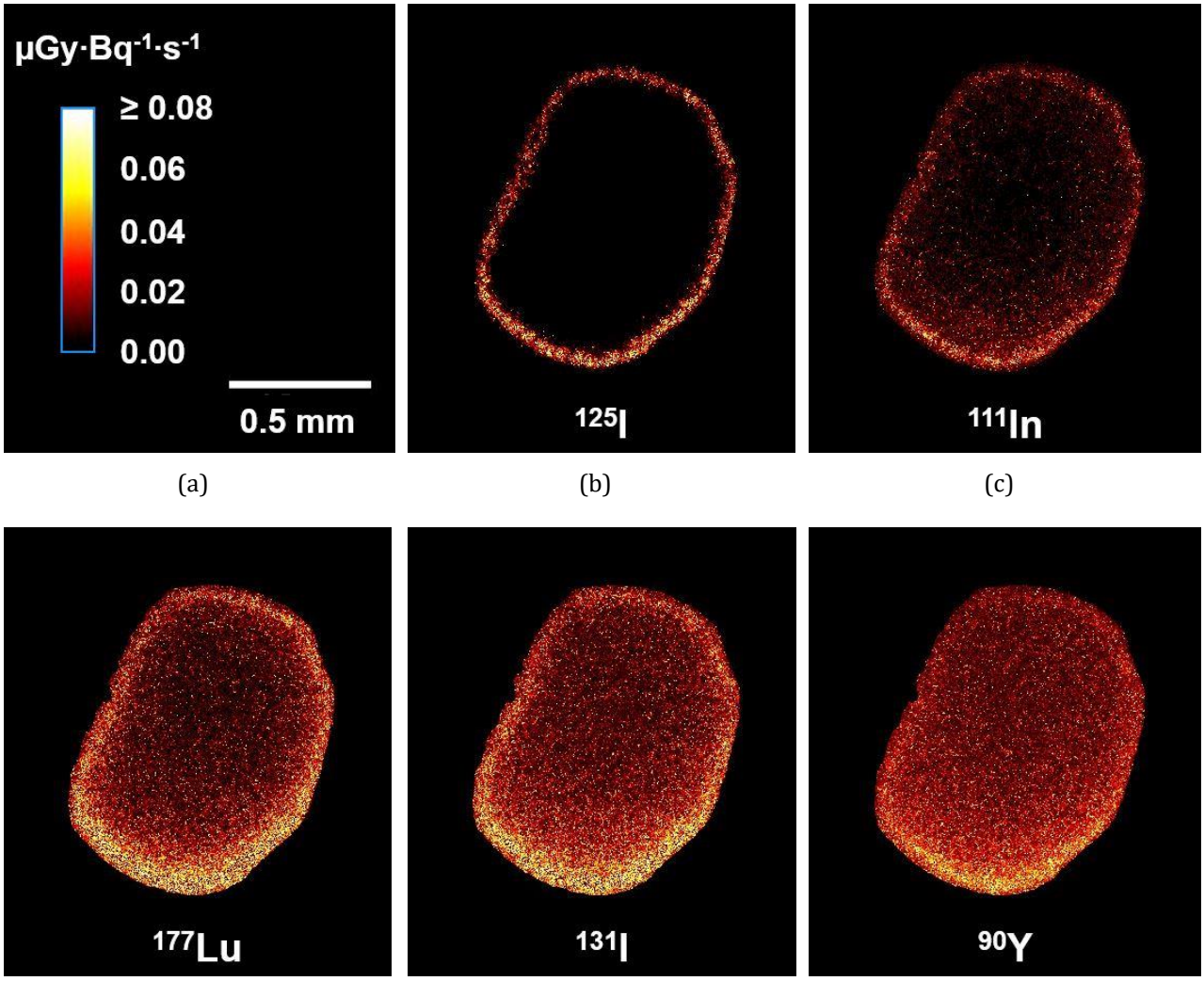

(a) (b) (c)

(d) (e) (f)

400 Figure 8. Absorbed dose per decay (μGy·Bq^{-1}·s^{-1}) delivered to the voxel of the slice of MALC D5 shown in Figure 1
401 (b), for (b) ^{125}I, (c) ^{111}In, (d) ^{177}Lu, (e) ^{131}I and (f) ^{90}Y. The corresponding color scale is displayed in (a).

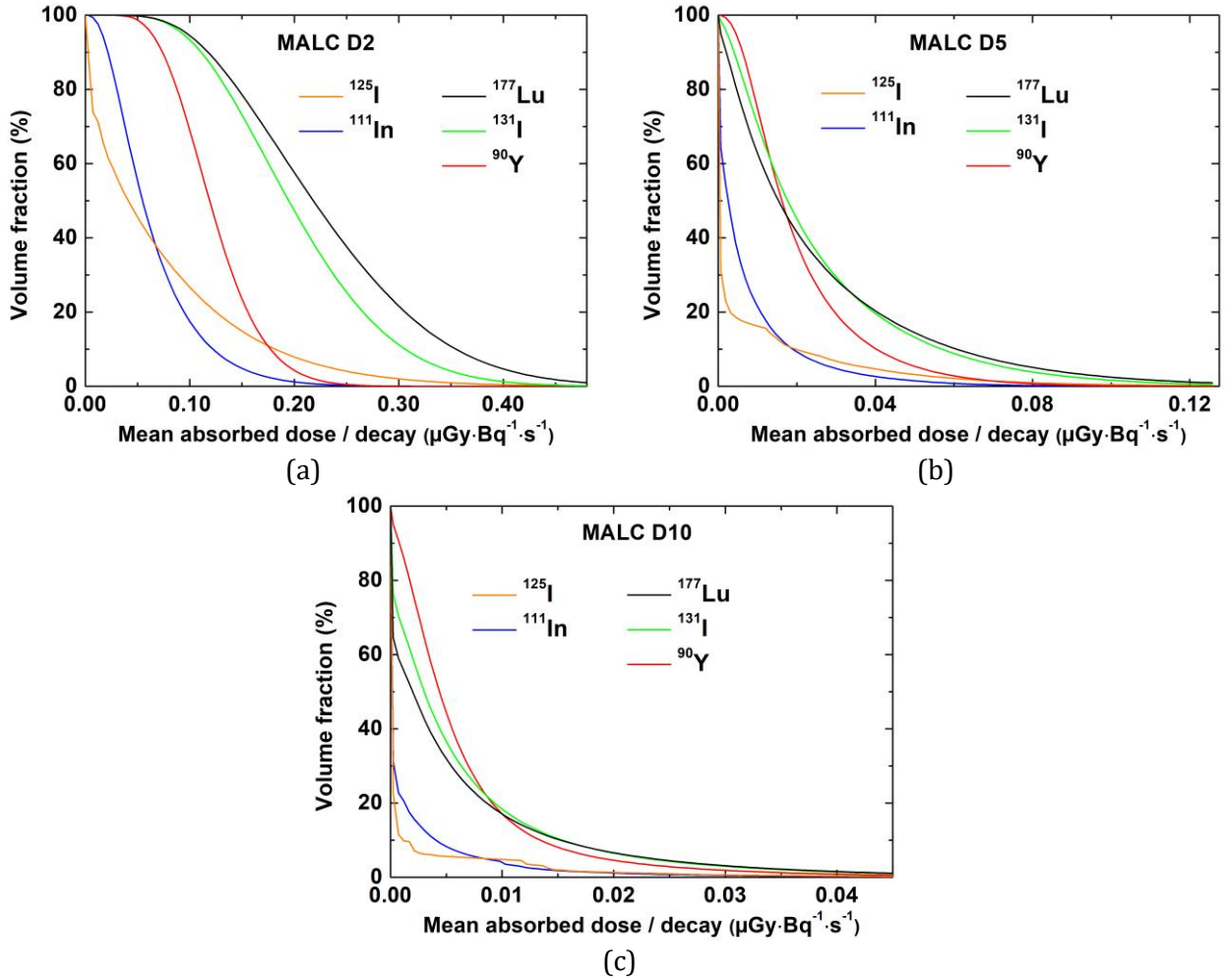

402 Figure 9. cDVH of MALC (a) D2, (b) D5 and (c) D10 per decay for ^{125}I, ^{111}In, ^{177}Lu, ^{131}I and ^{90}Y.

403

404 **3.3 Absorbed dose per unit administered activity**

405 The influence of the radiolabeled rituximab effective half-life on the absorbed dose is presented.

406 Table 6 summarizes the effective half-lives for radiolabeling with ^{125}I, ^{111}In, ^{177}Lu, ^{131}I or ^{90}Y as calculated

407 from equation (6). The differences between the physical half-lives of the radionuclides were decreased

408 by the introduction of the biological half-life of the rituximab (5.8 days).

409 Table 6. Effective half-lives of rituximab radiolabeled with one of the five radionuclides in NHL, determined with
410 equation (6).

Radionuclide X	Effective half-life of X-rituximab (day)
^{125}I	5.3
^{111}In	1.9
^{177}Lu	3.1
^{131}I	3.4
^{90}Y	1.8

411

412 For each radionuclide, Figure 10 displays the mean absorbed dose per unit administered activity
413 within the MALCs and Table 7 shows the corresponding numerical values. Regarding Auger electron
414 emitters, the effective half-life of ^{125}I-rituximab was 2.8 times higher than ^{111}In-rituximab. Therefore,
415 despite lower absorbed dose delivered per decay in MALC D5 and D10, ^{125}I delivered more absorbed
416 dose per unit administered activity than ^{111}In. For β^- particle emitters, the effective half-life of ^{177}Lu-
417 rituximab and ^{131}I-rituximab were 1.7 and 1.9 times greater than that of ^{90}Y-rituximab. As a result, ab-
418 sorbed dose per unit administered activity for ^{177}Lu and ^{131}I were more than 3 times higher in MALC D2
419 and more than 2 times higher in MALC D5 than that of ^{90}Y. Furthermore, in MALC D10, despite higher
420 absorbed dose per decay, ^{90}Y delivered less absorbed dose per unit administered activity than ^{177}Lu and
421 ^{131}I. As discussed by Scheidhauer *et al.*[58], the relatively long biological half-life of rituximab (5.8 days in
422 NHL) is best matched by ^{131}I physical half-life (8.0 days) than by ^{90}Y short physical half-life (2.7 days).
423 ^{177}Lu physical half-life of 6.6 days is also well adapted to the rituximab biological half-life.

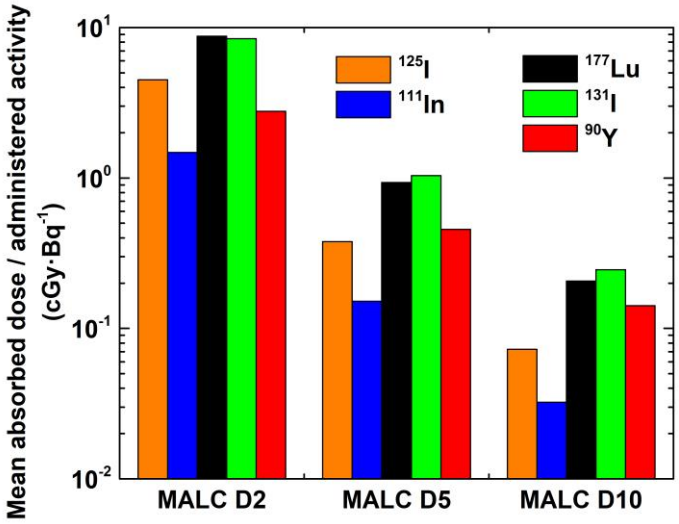

Figure 10. Mean absorbed dose per unit administered activity to MALCs D2, D5 and D10 for ^{125}I, ^{111}In, ^{177}Lu, ^{131}I and ^{90}Y.

Table 7. Mean absorbed dose per unit administered activity to the MALCs for the five radionuclides.

	Mean absorbed dose per unit administered activity (cGy · Bq^{-1})		
Radionuclide	**MALC D2**	**MALC D5**	**MALC D10**
^{125}I	4.50	$3.78 \cdot 10^{-1}$	$7.27 \cdot 10^{-2}$
^{111}In	1.48	$1.51 \cdot 10^{-1}$	$3.23 \cdot 10^{-2}$
^{177}Lu	8.76	$9.33 \cdot 10^{-1}$	$2.06 \cdot 10^{-1}$
^{131}I	8.45	1.04	$2.46 \cdot 10^{-1}$
^{90}Y	2.78	$4.56 \cdot 10^{-1}$	$1.42 \cdot 10^{-1}$

Figure 11 illustrates, as an example the isodoses (in cGy·Bq^{-1}) inside the voxels of the slice of MALC D5 shown by Figure 1 (b). Only the β^- particle emitters were represented since the absorbed dose distribution of Auger electron emitters were very heterogeneous and did not allow for a clear representation of isodoses. Figure 12 shows the cDVH of MALC (a) D2, (b) D5 and (c) D10 per unit administered activity for ^{125}I, ^{111}In, ^{177}Lu, ^{131}I and ^{90}Y.

When the effective half-life of radiolabeled rituximab increases, the absorbed doses per administered activity increase. As a consequence, the region covered by high absorbed dose is largest for ^{131}I and smallest for ^{90}Y as illustrated by the isodoses (Figure 11). Furthermore, the higher the effective half-

life, the greater the shift of the cDVH curves toward higher absorbed doses. Accordingly, in the region of high absorbed doses, cDVH values of ^{125}I become significantly higher than that of ^{111}In. In this region, cDVH values of ^{177}Lu and ^{131}I are noticeably higher than those of ^{90}Y.

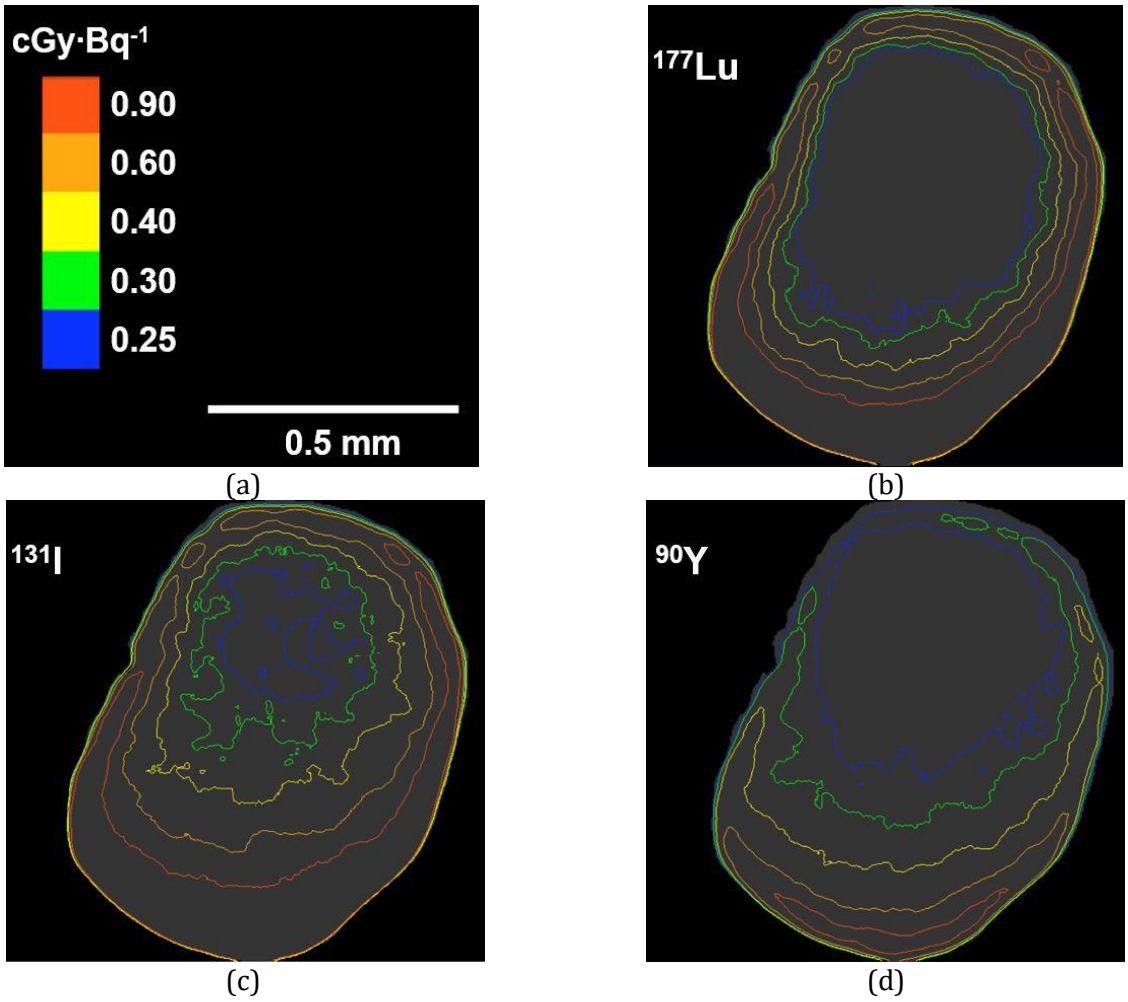

Figure 11. Isodose distributions in the slice of MALC D5 shown in Figure 1 (b), per unit administered activity of (b) ^{177}Lu, (c) ^{131}I and (d) ^{90}Y (cGy·Bq^{-1}). The corresponding color scale is displayed in (a).

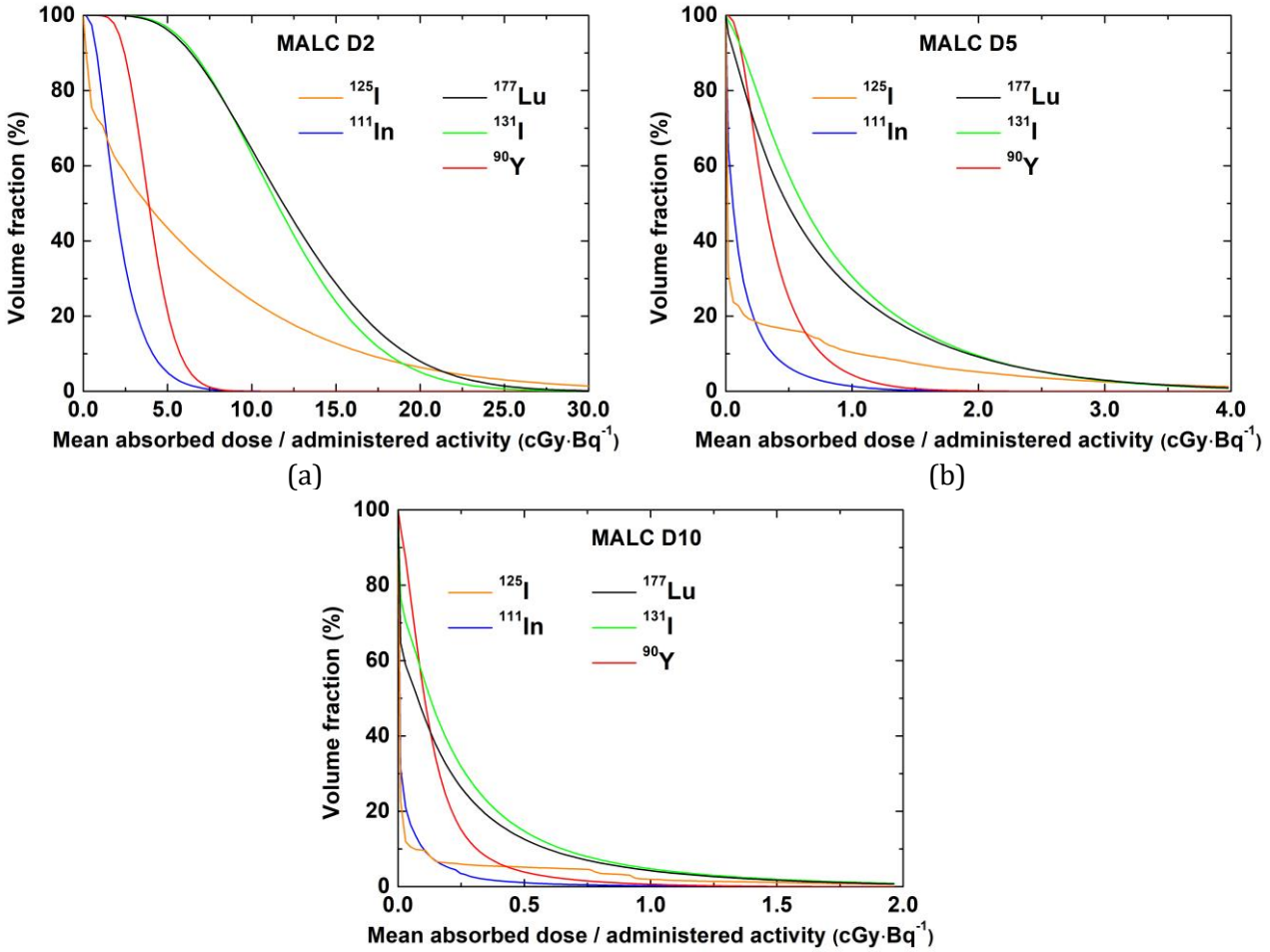

Figure 12. cDVH per unit administered activity of MALC (a) D2, (b) D5 and (c) D10 for ^{125}I, ^{111}In, ^{177}Lu, ^{131}I and ^{90}Y.

3.4 Discussion

Our methodology allowed the observation of the absorbed dose in an *in vitro* tumor model which is more realistic than the spherical tumor with uniform biodistribution simplification. It is recognized, however, that the realism of this work is limited with respect to clinical context. It is therefore essential to review the degree of relevance of the biological and physical aspects of this work.

The present study focused on three MALCs with dimensions of the order of millimeter. On one hand, such a sample did not reproduce the diversity of tumor geometry and rituximab pharmacokinetics in patients, which are critical for dosimetry. For example, in clinical routine, the size of the diagnosed follicular lymphomas ranges from a few millimeters to several centimeters[62]. Additionally, multiple studies have highlighted the need for dosimetry in smaller follicular lymphomas (down to ~10 µm)[63-65]. Our study did not extend to the biggest and the smallest of the follicular lymphomas. It is expected that, with the increasing / decreasing size of the tumor model, radionuclides with higher (*e.g.* ^{90}Y) / lower

458 (*e.g.* ^{125}I) penetration emissions, would become more favored from a dosimetric perspective. On the
459 other hand, previous studies have highlighted the ability of three-dimensional aggregates to mimic the
460 physiological *in vivo* aspects of tumors, enabling the identification of new targets and drugs[66-68]. In par-
461 ticular, this tool has long been recognized as very effective to characterize the penetration of antibod-
462 ies[69-70]. These previous works give confidence in the clinical relevance of the rituximab peripheral dis-
463 tribution in the MALCs, a key point of the present study.

464 The accurate Monte Carlo tracking of the radionuclide emissions in the MALCs relied largely on
465 the choice of the physics models. Geant4-DNA provides two sets of physics models able to entirely sim-
466 ulate the electron emissions of ^{125}I and ^{111}In: the default ("option 2") and the CPA100 ("option 6") sets.
467 The latter set was selected following two main arguments. Differential cross sections for ionization and
468 cross section for electronic excitation of "option 6" are in better agreement than that of "option 2" with
469 experimental data. Furthermore, for low energy electrons, dose-point kernels generated by "option 2"
470 are considered unrealistic because they are very diffusive[71], while those calculated by "option 6" are less
471 so[72]. Concerning β^- particle emitters, "Livermore" were considered more relevant than "PENELOPE-
472 2008"[73] electron physics models based on two arguments. Firstly, to be in accordance with Geant4-DNA
473 "option 6", the simulations were realized in liquid water. For this material, "Livermore" ionization cross
474 sections are in better agreement with experimental data[36]. Secondly, regarding deexcitation processes,
475 "Livermore" simulates every atomic shell, while "PENELOPE-2008" only takes into account K, L and M
476 shells[73].

477 Monte Carlo simulations were informed with data from one SPIM acquisition, showing biodis-
478 tribution in MALCs after 24 h of incubation. To approximate the time-dependent activity in the MALCs,
479 we used the straightforward assumptions of a radiopharmaceutical instantaneous uptake and monoex-
480 ponential elimination. In clinical studies, a more detailed description of the uptake and elimination is
481 provided. Typically, 3 to 4 SPECT or PET acquisitions are performed, the first a few hours and the last
482 between a few tenth of hours and nearly 200 h after administration[25,56,74-75]. Generally, these data are
483 fitted by a mono/biexponential function. The instantaneous uptake does not account for the decays oc-
484 curring outside the tumor during the uptake in a clinical context. Hence, the absorbed dose to the tumor

485 delivered by radionuclides with short half-lives, such as ^{111}In and ^{90}Y, is overestimated compared to
486 those with longer half-live. We note, however, that SPECT acquisitions of mice and patients showed early
487 uptake of rituximab in NHL[76-77] (a few hours after administration while ^{111}In and ^{90}Y physical half-lives
488 are ~2 days). Regarding the elimination of the rituximab in NHL, no data were found in the literature.
489 Implementation of more sophisticated pharmacokinetic models in our methodology would be an im-
490 portant next step for a more relevant dosimetry. Ideally, these models should consider rituximab data
491 in patients' NHL, upon availability.

492 **4 Conclusion**

493 We have developed a Monte Carlo dosimetric model based on realistic NHL geometry and ritux-
494 imab biodistribution. It was employed to describe the absorbed dose that would be delivered at the
495 microscopic scale by Auger electron emitters (^{125}I and ^{111}In) and β^- particle emitters (^{177}Lu, ^{131}I and ^{90}Y)
496 in the context of RIT.

497 A comparison between the mean absorbed dose per decay for realistic geometry and biodistri-
498 bution with literature data for a sphere with either a surface or a volume biodistribution demonstrated
499 significant differences. Then, for the five radionuclides, the absorbed fractions, the mean absorbed dose
500 and its associated distribution were compared. This comparison further highlighted the importance of
501 both the realistic MALC geometry and rituximab biodistribution as they often impacted the outcomes.

502 Aside from these two parameters, the decay properties - the electron / β^- particle energy re-
503 leased per decay and penetration - had an important impact. The uniformity of the absorbed dose deliv-
504 ered throughout the MALCs increased for radionuclides releasing more energy per decay (in ascending
505 order: ^{125}I, ^{111}In, ^{177}Lu, ^{131}I and ^{90}Y). The mean absorbed dose of β^- particle emitters was higher than that
506 of Auger electron emitters. ^{177}Lu and ^{131}I mean absorbed doses and were higher than ^{90}Y in the two
507 smallest MALCs. Furthermore, when considering the radiolabeled rituximab effective half-life, the ab-
508 sorbed dose for ^{177}Lu and ^{131}I remained close to each other and considerably greater than that of ^{90}Y in
509 the three MALCs.

510 The methodology developed may be applied to various situations of TRT. Voxelized images of
511 others tumoral / healthy tissue models and tumor-seeking agents can be considered. It is possible to

simulate the emission of other radionuclides of interest such as potential theranostic Auger electron emitters (*e.g.* copper-64[74], useful for PET imaging) and β- particle emitters (*e.g.* terbium-161[78-79], useful for SPECT imaging) or therapeutic α particle emitters (*e.g.* actinium-225[80-81]). To further improve the realism of the simulations, future work may integrate the temporal variation of the vector biodistribution and the growth of MALC. Such work could be useful in the case of real irradiation experiment to select relevant radionuclides and assess biological effects.

5 References

1. Strand SE, Jönsson BA, Ljungberg M, Tennvall J. Radioimmunotherapy dosimetry-a review. *Acta Oncol*. 1993;32(7-8):807-817. doi:10.3109/02841869309096140

2. Roeske JC, Aydogan B, Bardiès M, Humm JL. Small-scale dosimetry: challenges and future directions. *Semin Nucl Med*. 2008;38(5):367-383. doi:10.1053/j.semnuclmed.2008.05.003

3. Bardiès M, Chatal JF. Absorbed doses for internal radiotherapy from 22 beta-emitting radionuclides: beta dosimetry of small spheres. *Phys Med Biol*. 1994;39(6):961-981. doi:10.1088/0031-9155/39/6/004

4. Falzone N, Fernández-Varea JM, Flux G, Vallis KA. Monte Carlo evaluation of Auger electron-emitting theragnostic radionuclides. *J Nucl Med*. 2015;56(9):1441-1446. doi:10.2967/jnumed.114.153502

5. Champion C, Quinto MA, Morgat C, Zanotti-Fregonara P, Hindié E. Comparison between three promising β-emitting radionuclides, ^{67}Cu, ^{47}Sc and ^{161}Tb, with emphasis on doses delivered to minimal residual disease. *Theranostics*. 2016;6(10):1611-1618. doi:10.7150/thno.15132

6. Hindié E, Zanotti-Fregonara P, Quinto MA, Morgat C, Champion C. Dose deposits from ^{90}Y, ^{177}Lu, ^{111}In, and ^{161}Tb in micrometastases of various sizes: implications for radiopharmaceutical therapy. *J Nucl Med*. 2016;57(5):759-764. doi:10.2967/jnumed.115.170423

7. Amato E, Italiano A, Baldari S. An analytical model to calculate absorbed fractions for internal dosimetry with alpha, beta and gamma emitters. *Pericol Classe Sci Fis Mat Nat.* 2014;92(1):A1. doi:10.1478/AAPP.921A1

8. Amato E, Lizio D, Baldari S. Absorbed fractions for electrons in ellipsoidal volumes. *Phys Med Biol.* 2011;56(2):357-365. doi:10.1088/0031-9155/56/2/005

9. Rahman Z, Mirza SM, Arshed W, Mirza NM, Ahmed W. Influence of thyroid volume reduction on absorbed dose in ^{131}I therapy studied by using Geant4 Monte Carlo simulation. *Chin Phys C*. 2014;38(87):056201. doi:10.1088/1674-1137/38/5/056201

10. Bao A, Zhao X, Phillips WT, et al. Theoretical study of the influence of a heterogeneous activity distribution on intratumoral absorbed dose distribution. *Med Phys*. 2005;32(1):200-208. doi:10.1118/1.1833151

11. Spaic R, Ilic R, Dragovic M, Petrovic B. Generation of dose-volume histograms using Monte Carlo simulations on a multicellular model in radionuclide therapy. *Cancer Biother Radio*. 2005;20(3):320-324. doi:10.1089/cbr.2005.20.320

12. Uusijärvi H, Bernhardt P, Forssell-Aronsson E. Tumour control probability (TCP) for non-uniform activity distribution in radionuclide therapy. *Phys Med Biol*. 2008;53(16):4369-4381. doi:10.1088/0031-9155/53/16/010

13. Howell RW , Rajon D, Bolch BE. Monte Carlo simulation of irradiation and killing in three-dimensional cell-populations with lognormal cellular uptake of radioactivity. *Int J Radiat Biol*. 2012;88(1-2):115-122. doi:10.3109/09553002.2011.602379

14. Arnaud FX, Paillas S, Pouget JP, Incerti S, Bardiès M, Bordage MC. Complex cell geometry and sources distribution model for Monte Carlo single cell dosimetry with iodine 125 radioimmunotherapy. *Nucl Instrum Methods Phys Res B.* 2016;366:227-233. doi:10.1016/j.nimb.2015.11.008

15. Daydé D, Ternant D, Ohresser M, et al. Tumor burden influences exposure and response to rituximab: pharmacokinetic-pharmacodynamic modeling using a syngeneic bioluminescent murine model expressing human CD20. *Blood*. 2009;113(16):3765-3772. doi:10.1182/blood-2008-08-175125

16. Meignan M, Cottereau AS, Versari A, et al. Baseline metabolic tumor volume predicts outcome in high-tumor-burden follicular lymphoma: a pooled analysis of three multicenter studies. *J Clin Oncol*. 2016;34(30):3618-3626. doi:10.1200/JCO.2016.66.9440

17. Netti PA, Berk DA, Swartz MA, Grodzinsky AJ, Jain RK. Role of extracellular matrix assembly in interstitial transport in solid tumors. *Cancer Res*. 2000;60(9):2497-2503.

18. Gravelle P, Jean C, Valleron W, Laurent G, Fournié JJ. Innate predisposition to immune escape in follicular lymphoma cells. *Oncoimmunology*. 2012;1(4):555-556. doi:10.4161/onci.19365

19. Gravelle P, Jean C, Familiades J, et al. Cell growth in aggregates determines gene expression, proliferation, survival, chemoresistance, and sensitivity to immune effectors in follicular lymphoma. *Am J Pathol*. 2014;184(1):282-295. doi:10.1016/j.ajpath.2013.09.018

20. Decaup E, Jean C, Laurent C, et al. Anti-tumor activity of obinutuzumab and rituximab in a follicular lymphoma 3D model. *Blood Cancer J*. 2013;3(8):e131. doi:10.1038/bcj.2013.32

21. Rossi C, Gravelle P, Decaup E, et al. Boosting γδ T cell-mediated antibody-dependent cellular cytotoxicity by PD-1 blockade in follicular lymphoma. *Oncoimmunology*. 2019;8(3):1554175. doi:10.1080/2162402X.2018.1554175

22. Read ED, Eu P, Little PJ, Piva TJ. The status of radioimmunotherapy in CD20+ non-Hodgkin's lymphoma. *Target Oncol*. 2015;10(1):15-26. doi:10.1007/s11523-014-0324-y

23. Griffiths GL, Govindan SV, Sgouros G, Ong GL, Goldenberg DM, Mattes MJ. Cytotoxicity with Auger electron-emitting radionuclides delivered by antibodies. *Int J Cancer*. 1999;81(6):985-992. doi:10.1002/(SICI)1097-0215(19990611)81:6<985::AID-IJC23>3.0.CO;2-W

24. Ong GL, Elsamra SE, Goldenberg DM, Mattes MJ. Single-cell cytotoxicity with radiolabeled antibodies. *Clin Cancer Res*. 2001;7(1):192-201.

25. Blakkisrud J, Løndalen A, Martinsen ACT, et al. Tumor-absorbed dose for non-Hodgkin lymphoma patients treated with the anti-CD37 antibody radionuclide conjugate ^{177}Lu-lilotomab satetraxetan. *J Nucl Med*. 2017;58(1):48-54. doi:10.2967/jnumed.116.173922

26. Goldsmith SJ. Radioimmunotherapy of lymphoma: Bexxar and Zevalin. *Semin Nucl Med*. 2010;40(2):122-135. doi:10.1053/j.semnuclmed.2009.11.002

27. Bezombes C, Grazide S, Garret C, et al. Rituximab antiproliferative effect in B-lymphoma cells is associated with acid-sphingomyelinase activation in raft micodomains. *Blood*. 2004;104(4):1166-1173. doi:10.1182/blood-2004-01-0277

28. Huisken J, Stainier DYR. Selective plane illumination microscopy techniques in developmental biology. *Development*. 2009;136(12):1963-1975. doi:10.1242/dev.022426

29. Ichikawa T, Nakazato K, Keller PJ, et al. Live imaging and quantitative analysis of gastrulation in mouse embryos using light-sheet microscopy and 3D tracking tools. *Nat Protoc*. 2014;9(3):575-585. doi:10.1038/nprot.2014.035

30. Weber M, Mickoleit M, Huisken J. Multilayer mounting for long-term light sheet microscopy of zebrafish. *J Vis Exp*. 2014;(84):e51119. doi:10.3791/51119

31. Schindelin J, Arganda-Carreras I, Frise E, et al. Fiji: an open source platform for biological image analysis. *Nat Methods*. 2012;9(7):676-682. doi:10.1038/nmeth.2019

32. Eliceiri KW, Rueden C. Tools for visualizing multidimensional images from living specimens. *Photochem Photobiol*. 2005;81(5):1116-1122. doi:10.1562/2004-11-22-IR-377

33. Sugiura G, Kühn H, Sauter M, Haberkorn U and Mier W. Radiolabeling strategies for tumor-targeting proteinaceous drugs. *Molecules.* 2014;19(2):2135-2165. doi:10.3390/molecules19022135

34. Agostinelli S, Allison J, Amako K, et al. Geant4—a simulation toolkit. *Nucl Instrum Methods Phys Res A.* 2003;506(3). doi:10.2172/799992

35. Allison J, Amako K, Apostolakis J, et al. Geant4 developments and applications. *IEEE Trans Nuc. Sci* 2006;53(1):270-278. doi:10.1109/TNS.2006.869826

36. Allison J, Amako K, Apostolakis J, et al. Recent developments in Geant4. *Nucl Instrum Methods Phys Res A* 2016;835:186-225. doi:10.1016/j.nima.2016.06.125

37. Incerti S, Seznec H, Simon M, Barberet P, Habchi C, Moretto P. Monte Carlo dosimetry for targeted irradiation of individual cells using a microbeam facility. *Radiat Prot Dosim.* 2009;133(1):2-11.

38. Barberet P, Vianna F, Karamitros M, et al. Monte-Carlo dosimetry on a realistic cell monolayer geometry exposed to alpha particles. *Phys Med Biol*. 2012;57(8):2189-2207. doi:10.1088/0031-9155/57/8/2189

39. Howell RW. Radiation spectra for Auger electrons emitting radionuclides: Report No. 2 of AAPM Nuclear Medicine Task Group No 6. *Med Phys.* 1992;19(6) 1371-1383. doi:10.1118/1.596927

40. Taborda A, Benabdallah N, Desbrée A. Dosimetry at the sub-cellular scale of Auger-electron emitter ^{99m}Tc in a mouse single thyroid follicle. *Appl Radiat Isot*. 2016;108:58-63. doi:10.1016/j.apradiso.2015.12.010

41. Piroozfar B, Raisali G, Alirezapour B, Mirzaii M. The effect of ^{111}In radionuclide distance and Auger electron energy on direct induction of DNA double-strand breaks: a Monte Carlo study using Geant4 toolkit. *Int J Radiat Biol*. 2018;94(4):385-393. doi:10.1080/09553002.2018.1440329

42. Eckerman K, Endo A. *MIRD: Radionuclide data and decay schemes.* Reston, VA: Society for Nuclear Medicine; 2008.

43. Kassis AI. The amazing world of Auger electrons. *Int J Radiat Biol*. 2004;80(11-12):789-803. doi:10.1080/09553000400017663

44. Bernal MA, Bordage MC, Brown JMC, et al. Track structure modeling in liquid water: A review of the Geant4-DNA very low energy extension of the Geant4 Monte Carlo simulation toolkit. *Phys Med*. 2015;31(8):861-874. doi:10.1016/j.ejmp.2015.10.087

45. Incerti S, Ivanchenko A, Karamitros M, et al. Comparison of GEANT4 very low energy cross section models with experimental data in water. *Med Phys*. 2010;37(9):4692-4708. doi:10.1118/1.3476457

46. Incerti S, Baldacchino G, Bernal M, et al. The Geant4-DNA project. *Int J Model Simul Sci Comput*. 2010;1(2):157-178. doi:10.1142/S1793962310000122

47. Incerti S, Kyriakou I, Bernal MA, et al. Geant4-DNA example applications for track structure simulations in liquid water: a report from the Geant4-DNA Project. *Med Phys*. 2018;45(8):e722-e739. doi:10.1002/mp.13048

48. Bordage MC, Bordes J, Edel S, et al. Implementation of new physics models for low energy electrons in liquid water in Geant4-DNA. *Phys Med*. 201632(12):1833-1840. doi:10.1016/j.ejmp.2016.10.006

49. Bordes J. Low-energy electron transport with alternative physics models within Geant4-DNA code and radioimmunotherapy applications [dissertation]. Toulouse, France: Toulouse III-Paul Sabatier University; 2017.

50. Cullen DE, Hubbell JH, Kissel L, Laboratory LLN. EPDL97: the evaluated photon data library `97 version. *Livermore, CA: Lawrence Livermore National Laboratory.* 1997;Report UCLR--50400 Vol.6-Rev.(5). doi:10.2172/295438

51. Ivanchenko VN, Incerti S, Francis Z, et al. Combination of electromagnetic physics processes for microdosimetry in liquid water with the Geant4 Monte Carlo simulation toolkit. *Nucl Instrum Methods Phys Res B*. 2012;273:95-97. doi:10.1016/j.nimb.2011.07.048

52. Perkins ST, Cullen DE, Seltzer SM. Tables and graphs of electron-interaction cross sections from 10 eV to 100 GeV derived from the LLNL Evaluated Electron Data Library (EEDL), Z = 1--100. *Livermore, CA: Lawrence Livermore National Laboratory.* 1991;Report UCLR--50400 Vol. 31:21-24. doi:10.2172/5691165

53. Perkins ST, Cullen DE, Chen MH, Rathkopf J, Scofield J, Hubbell JH. Tables and graphs of atomic subshell and relaxation data derived from the LLNL Evaluated Atomic Data Library (EADL), Z= 1--100. *Livermore, CA: Lawrence Livermore National Laboratory.* 1991;Report UCLR--50400 Vol. 30. doi:10.2172/10121422

54. Loevinger R, Budinger TF, Watson EE. *MIRD primer for absorbed dose calculations*. New York: Society of Nuclear Medicine; 1988.

55. Bolch WE, Eckerman KF, Sgouros G, Thomas SR. MIRD Pamphlet No. 21: a generalized schema for radiopharmaceutical dosimetry—standardization of nomenclature. *J Nucl Med*. 2009;50(3):477-484. doi:10.2967/jnumed.108.056036

56. Ljungberg M, Sjögreen-Gleisner K. The accuracy of absorbed dose estimates in tumours determined by quantitative SPECT: a Monte Carlo study. *Acta Oncol*. 2011;50(6):981-989. doi:10.3109/0284186X.2011.584559

57. Marcatili S, Villoing D, Mauxion T, McParland BJ, Bardiès M. Model-based versus specific dosimetry in diagnostic context: comparison of three dosimetric approaches. *Med Phys*. 2015;42(3):1288-1296. doi:10.1118/1.4907957

58. Scheidhauer K, Wolf I, Baumgartl HJ, et al. Biodistribution and kinetics of ^{131}I-labelled anti-CD20 MAB IDEC-C2B8 (rituximab) in relapsed non-Hodgkin's lymphoma. *Eur J Nucl Med Mol Imaging*. 2002;29(10):1276-1282. doi:10.1007/s00259-002-0820-7

59. Gustafsson J, Brolin G, Cox M, Ljungberg M, Johansson L and Sjögreen Gleisner K. Uncertainty propagation for SPECT/CT-based renal dosimetry in ^{177}Lu peptide receptor radionuclide therapy. *Phys Med Biol*. 2015;60(21):8329-8346. doi:10.1088/0031-9155/60/21/8329

60. Gear JI, Cox MG, Gustafsson J, et al. EANM pratical guidance on uncertainty analysis for molecular radiotherapy absorbed dose calculations. *Eur J Nucl Med Mol Imaging*. 2018;45(13):2456-2474. doi:10.1007/s00259-018-4136-7

61. Berger MJ, Coursey JS, Zucker MA, Chang J. ESTAR, PSTAR, and ASTAR: computer programs for calculating stopping-power and range tables for electrons, protons, and helium ions (version 1.2.3). *Gaithersburg, MD: NIST*. 2005;Technical Report NISTIR 4999. https://www.nist.gov/pml/stopping-power-range-tables-electrons-protons-and-helium-ions. Accessed October 9, 2018.

62. Wilder RB, Jones D, Tucker SL, et al. Long-term results with radiotherapy for stage I-II follicular lymphomas. *Int J Radiat Oncol Biol Phys*. 2001;51(5):1219-1227. doi:10.1016/s0360-3016(01)01747-3

63. Bousis C, Emfietzoglou D, Hadjidoukas P and Nikjoo H. Monte Carlo single-cell dosimetry of Auger-electron emitting radionuclide. *Phys Med Biol*. 2010;55(9):2555-2572. doi:10.1088/0031-9155/55/9/009

64. Bousis C, Emfietzoglou D and Nikjoo H. Monte Carlo single-cell dosimetry of I-131, I-125 and I-123 for targeted radioimmunotherapy of B-cell lymphoma. *Int J Radiat Biol*. 2012;88(12):908-915. doi:10.3109/09553002.2012.666004

65. Fourie H, Newman RT and Slabbert JP. Microdosimetry of the Auger electron emitting ^{123}I radionnuclide using Geant4-DNA simulations. *Phys Med Biol*. 2015;60(8):3333-3346. doi:10.1088/0031-9155/60/8/3333

66. Duval K, Grover H, Han LH, et al. Modeling physiological events in 2D vs. 3D cell culture. *Physiology*. 2017;32(4):266-277. doi:10.1152/physiol.00036.2016

67. Thoma CR, Zimmermann M, Agarkova I, Kelm JM and Krek W. 3D cell culture systems modeling tumor growth determinants in cancer target discovery. *Adv Drug Deliv Rev*. 2014;69-70:29-41. doi:10.1016/j.addr.2014.03.001

68. Hirschhaeuser F, Menne H, Dittfeld C, West J, Mueller-Klieser W and Kunz-Schughart LA. Multicellular tumor spheroids: An underestimated tool is catching up again. *J Biotechnol*. 2010;148(1):3-15. doi:10.1016/j.jbiotec.2010.01.012

69. Sutherland R, Buchegger F, Schreyer M, Vacca A and Mach JP. Penetration and binding of radiolabeled anti-carcinoembryonic antigen monoclonal antibodies and their antigen binding fragments in human colon multicellular tumor spheroids. *Cancer Res*. 1987;47(6):1627-1633.

70. Minchinton AI, Tannock IF. Drug penetration in solid tumors. *Nat Rev Cancer*. 2006;6(8):583-592. doi:10.1038/nrc1893

71. Kyriakou I, Incerti S, Francis Z. Technical Note: Improvements in GEANT4 energy-loss model and the effect on low-energy electron transport in liquid water. *Med Phys*. 2015;42(7):3870-3876. doi:10.1118/1.4921613

72. Bordes J, Incerti S, Lampe N, Bardiès M, Bordage MC. Low-energy electron dose-point kernel simulations using new physics models implemented in Geant4-DNA. *Nucl Instrum Methods Phys Res B*. 2017;398:13-20. doi:10.1016/j.nimb.2017.02.044

73. Salvat F, Fernández-Varea JM, Sempau J. PENELOPE-2008: a code system for Monte Carlo simulation of electron and photon transport. *Issy-les-Moulineaux, France: OECD-NEA*. 2009;Report 6416. https://www.oecd-nea.org/science/pubs/2009/nea6416-penelope.pdf. Accessed Decembre 1st, 2019.

74. Avila-Rodriguez MA, Rios C, Carrasco-Hernandez J, et al. Biodistribution and radiation dosimetry of [^{64}Cu]copper dichloride: first-in-human study in healthy volunteers. *EJNMMI Res*. 2017;7(1). doi:10.1186/s13550-017-0346-4

75. Santoro L, Mora-Ramirez E, Trauchessec D, et al. Implementation of patient dosimetry in the clinical practice after targeted radiotherapy using [^{177}Lu-[DOTA0, Tyr3]-octreotate. *EJNMMI Res.* 2018;8(1):103. doi:10.1186/s13550-018-0459-4

76. Camacho X, Machado CL, García MF, et al. Technetium-99m- or Cy7-labeled rituximab as an imaging agent for non-Hodgkin lymphoma. *Oncology*. 2017;92(4):229-242. doi:10.1159/000452419

77. Stopar TG, Fettich J, Zver S, et al. ^{99m}Tc-labelled rituximab, a new non-Hodgkin's lymphoma imaging agent: First clinical experience. *Nuc Med Commun*. 2008;29(12):1059-1065. doi:10.1097/MNM.0b013e3283134d6e

78. Müller C, van der Meulen NP, Benešová M, Schibli R. Therapeutic radiometals beyond ^{177}Lu and ^{90}Y: production and application of promising α-particle, β^--particle, and Auger electron emitters. *J Nucl Med*. 2017;58(Supplement 2):91S-96S. doi:10.2967/jnumed.116.186825

79. Müller C, Domnanich KA, Umbricht CA, van der Meulen NP. Scandium and terbium radionuclides for radiotheranostics: current state of development towards clinical application. *Br J Radiol.* 2018;91(1091):20180074. doi:10.1259/bjr.20180074

80. Kratochwil C, Bruchertseifer F, Rathke H, et al. Targeted α-therapy of metastatic castration-resistant prostate cancer with ^{225}Ac-PSMA-617: dosimetry estimate and empiric dose finding. *J Nucl Med*. 2017;58(10):1624-1631. doi:10.2967/jnumed.117.191395

81. Robertson AKH, Ramogida CF, Schaffer P, Radchenko V. Development of ^{225}Ac radiopharmaceuticals: TRIUMF perspectives and experiences. *Curr Radiopharm*. 2018;11(3):156-172. doi:10.2174/1874471011666180416161908

6 Acknowledgments

We would like to express our gratitude to Prof. Steve Archibald (PET Research Centre, University of Hull) and Dr Jean-Luc Gerner (ESA/ESTEC, retired) for helpful advice. We thank Lise Teyssedre (ITAV/CNRS) for fruitful discussion of SPIM imaging.

7 Conflict of interest statement

The authors declare that there is no conflict of interest regarding the publication of this article.